

# Observations of Multiple Blobs in Homologous Solar Coronal Jets in Closed Loop

Q.M. Zhang<sup>1</sup> · H.S. Ji<sup>1</sup> · Y.N. Su<sup>1</sup>

Received: 10 September 2015 / Accepted: 8 March 2016 / Published online: 18 March 2016  
© Springer Science+Business Media Dordrecht 2016

**Abstract** Coronal bright points (CBPs) and jets are ubiquitous small-scale brightenings that are often associated with each other. We here report our multiwavelength observations of two groups of homologous jets. The first group was observed by the *Extreme-Ultraviolet Imager* (EUVI) onboard the *Solar TERrestrial RELations Observatory* (STEREO) *Behind* spacecraft in 171 Å and 304 Å on 2014 September 10, from a location where no data from the *Solar Dynamic Observatory* (SDO) could be obtained. The jets (J1–J6) recurred for six times with intervals of 5–15 minutes. They originated from the same primary CBP (BP1) and propagated in the northeast direction along large-scale, closed coronal loops. Two of the jets (J3 and J6) produced sympathetic CBPs (BP2 and BP3) after reaching the remote footpoints of the loops. The time delays between the peak times of BP1 and BP2 (BP3) are  $240 \pm 75$  s ( $300 \pm 75$  s). The jets were not coherent. Instead, they were composed of bright and compact blobs. The sizes and apparent velocities of the blobs are 4.5–9 Mm and  $140$ – $380$  km s<sup>-1</sup>. The arrival times of the multiple blobs in the jets at the far end of the loops indicate that the sympathetic CBPs are caused by jet flows and not by thermal conduction fronts. The second group was observed by the *Atmospheric Imaging Assembly* onboard SDO in various wavelengths on 2010 August 3. Similar to the first group, the jets originated from a short-lived BP at the boundary of Active Region 11092 and propagated along a small-scale, closed loop before flowing into the active region. Several tiny blobs with sizes of  $\sim 1.7$  Mm and an apparent velocity of  $\sim 238$  km s<sup>-1</sup> were identified in the jets. We carried out differential emission measure (DEM) inversions to investigate the temperatures of the blobs, finding that the blobs were multithermal with an average temperature of 1.8–3.1 MK. The estimated number densities of the blobs were  $(1.7$ – $2.8) \times 10^9$  cm<sup>-3</sup>.

---

✉ Q.M. Zhang  
[zhangqm@pmo.ac.cn](mailto:zhangqm@pmo.ac.cn)

H.S. Ji  
[jihhs@pmo.ac.cn](mailto:jihhs@pmo.ac.cn)

Y.N. Su  
[yysu@pmo.ac.cn](mailto:yysu@pmo.ac.cn)

<sup>1</sup> Key Laboratory for Dark Matter and Space Science, Purple Mountain Observatory, CAS, Nanjing 210008, China

**Keywords** Flares, microflares and nanoflares · Magnetic reconnection, observational signatures · Jets

## 1. Introduction

Coronal jets are transient and collimated plasma motions accompanied by point-like or loop-like brightenings at their base. They were first discovered in soft X-ray (SXR) by *Yohkoh* spacecraft observations (Shibata *et al.*, 1992). With the development of solar space telescopes and the increase of spatial resolution, more and more coronal jets are observed and investigated in SXR as well as extreme-ultraviolet (EUV) wavelengths (Shimojo *et al.*, 1996; Shimojo and Shibata, 2000; Paraschiv, Bemporad, and Sterling, 2015; Nisticò *et al.*, 2015). They are located not only in coronal holes and along the active region (AR) boundary where open magnetic field dominates, but also in quiet regions with large-scale, closed magnetic field (Cirtain *et al.*, 2007; Culhane *et al.*, 2007; Zhang *et al.*, 2012). The typical length of jets is 10–400 Mm, the width is 5–100 Mm, and the apparent velocity is 10–1000 km s<sup>-1</sup> (Shimojo *et al.*, 1996). The temperature of polar jets ranges from 0.1 to 6.2 MK, with an average value of 1.8 MK. The electron number density of polar jets ranges from 0.1 to  $8.0 \times 10^8$  cm<sup>-3</sup>, with an average value of  $1.5 \times 10^8$  cm<sup>-3</sup> (Paraschiv, Bemporad, and Sterling, 2015). These parameters for polar jets are much lower than those for flare-related jets where much more free energy is released (Shimojo and Shibata, 2000). It is generally accepted that coronal jets are caused by magnetic reconnection. The way of reconnection, however, depends largely on the magnetic configuration. In the two-dimensional (2D) case, new magnetic fluxes emerge from beneath the photosphere and reconnect with the pre-existing, oppositely oriented open magnetic fields, resulting in hot, collimated jets and two bright lobes at the base of jets (Heyvaerts, Priest, and Rust, 1977; Shibata *et al.*, 1992; Yokoyama and Shibata, 1996). This mechanism became popular and was developed in modern three-dimensional (3D) magnetohydrodynamic (MHD) numerical experiments (Moreno-Insertis, Galsgaard, and Ugarte-Urra, 2008; Moreno-Insertis and Galsgaard, 2013; Archontis and Hood, 2013; Fang, Fan, and McIntosh, 2014). A fraction of rotating coronal jets might be produced by the magnetic reconnection as a result of the swirling motion of an embedded bipole in the photosphere (Pariat, Antiochos, and DeVore, 2009, 2010; Wyper and DeVore, 2015). Moore *et al.* (2010) classified coronal jets into the standard type and blowout type. The standard type with simpler morphology can be explained by the emerging-flux model (Shibata *et al.*, 1992; Lim *et al.*, 2016). The blowout type usually results from small-scale filament eruptions (Moore *et al.*, 2013). They have cool components and show rotating and/or transverse drifting motions (Chen, Zhang, and Ma, 2012; Hong *et al.*, 2013; Pucci *et al.*, 2013; Schmieder *et al.*, 2013; Zhang and Ji, 2014a; Liu *et al.*, 2015b). However, Sterling *et al.* (2015) proposed that both the standard and blowout polar jets in their sample were driven by small-scale filament eruptions, which resembled the coronal mass ejections (CMEs) driven by typical filament eruptions (Lin, 2004). Sometimes, a jet recurs at the same place with the same morphology and direction of outflow, forming the so-called recurrent or homologous jets. Recurrent jets may result from recurring magnetic reconnection (Chifor *et al.*, 2008; Innes, Cameron, and Solanki, 2011; Wang and Liu, 2012; Zhang *et al.*, 2012; Guo *et al.*, 2013; Chandra *et al.*, 2015), moving magnetic features (Yang *et al.*, 2013), continuous twisting motion of the photosphere (Pariat, Antiochos, and DeVore, 2010), emergence of a bipole below a transequatorial loop (Jiang *et al.*, 2013), or repeated cancellations of the pre-existing magnetic flux by the newly emerging flux (Chae *et al.*, 1999; Chen *et al.*, 2015; Li *et al.*, 2015).

For the first time, Zhang and Ji (2014b) reported the discovery of recurring blobs in homologous EUV jets observed by the *Atmospheric Imaging Assembly* (AIA; Lemen *et al.*, 2012) onboard the *Solar Dynamics Observatory* (SDO) with unprecedented temporal and spatial resolutions. Using six of the optically thin filters (94, 131, 171, 193, 211, 335 Å) of AIA, the authors performed the differential emission measure (DEM) inversion and derived the DEM profiles of the recurring blobs as a function of temperature. It is found that the bright and compact features with average size of  $\sim 3$  Mm are multithermal in nature with an average temperature of  $\sim 2.3$  MK. They are ejected outward along the jet flow at speeds of  $120\text{--}450$  km s $^{-1}$ . Most of the blobs have lifetimes of 24–60 s before merging with the background plasma and disappearing. Such intermittent magnetic plasmoids or blobs created by magnetic reconnection have also been observed in the large-scale current sheet (CS) driven by CMEs and the small-scale CS associated with chromospheric jets (Asai *et al.*, 2004; Lin *et al.*, 2005; Takasao *et al.*, 2012; Singh *et al.*, 2012; Kumar and Cho, 2013; Lin *et al.*, 2015). They are generally explained by the tearing-mode instability (TMI) of a thin CS, where a series of magnetic islands are recurrently created during magnetic reconnection (Furth, Killeen, and Rosenbluth, 1963; Drake *et al.*, 2006; Bárta, Vršnak, and Karlický, 2008; Innes *et al.*, 2015), which makes electron acceleration more efficient and dynamic (Kliem, Karlický, and Benz, 2000). Recently, multidimensional MHD numerical simulations of TMI have been significantly improved, thanks to the rapid advancement of powerful supercomputers. Yang *et al.* (2013) performed 2.5-dimensional (2.5D;  $\partial/\partial z = 0$ ) numerical experiments to simulate the process of magnetic reconnection between the moving magnetic features and the pre-existing magnetic field. The experiments successfully reproduced the plasmoids as a result of TMI, which are consistent with the observed bright moving blobs in the chromospheric anemone jets. The plasmoids have temperatures of  $\sim 0.015$  MK, densities of  $\sim 1.5 \times 10^{14}$  cm $^{-3}$ , and sizes of 0.05–0.15 Mm. They move bidirectionally at speeds of  $\sim 30$  km s $^{-1}$ , which is close to the local Alfvén speed. After reaching the outflow regions, the plasmoids collide with the magnetic fields there and are quickly destroyed as they disappear. Using a Harris CS, Ni *et al.* (2015) performed 2.5D numerical simulations of magnetic reconnection in the partially ionized chromosphere by considering the radiative loss and ambipolar diffusion due to the neutral–ion collisions. The reconnection rates (0.01–0.03), temperature ( $\sim 0.08$  MK), and upward outflow velocities ( $\sim 40$  km s $^{-1}$ ) of the plasmoids created by the plasmoid instability correspond well to their characteristic values in chromospheric jets.

Coronal jets are often associated with coronal bright points (CBPs) at their base (Krieger, Vaiana, and van Speybroeck, 1971; Golub *et al.*, 1974; Habbal and Withbroe, 1981; Zhang, Fang, and Zhang, 2012; Hong *et al.*, 2014; Alipour and Safari, 2015). As one type of long-lived (2–48 hr), small-scale ( $10''\text{--}40''$ ) activities with temperature (1–4 MK; Kariyappa *et al.*, 2011) and density ( $10^9\text{--}10^{10}$  cm $^{-3}$ ; Ugarte-Urra, Doyle, and Del Zanna, 2005) enhancements, CBPs are also believed to be heated by magnetic reconnection in the lower corona (*e.g.* Priest, Parnell, and Martin, 1994; Mandrini *et al.*, 1996; Longcope, 1998; Santos and Büchner, 2007). Likewise, the intensities of CBPs occasionally show periodic variations as a result of repeated and intermittent magnetic reconnections, with the period ranging from a few minutes to about one hour (Strong *et al.*, 1992; Tian, Xia, and Li, 2008; Kariyappa and Varghese, 2008; Zhang *et al.*, 2012; Ning and Guo, 2014; Samanta, Banerjee, and Tian, 2015). By performing a potential-field ( $\nabla \times \mathbf{B} = 0$ ) magnetic extrapolation, Zhang *et al.* (2012) found that two neighboring CBPs on 2007 March 16 were associated with two magnetic null points and the corresponding dome-shaped, spine–separatrix topology. Based on the magnetic configurations, the authors proposed that the CBP evolutions consist of quasi-periodic, impulsive flashes and gradual, weak brightening, which are caused

by fast null-point reconnection and slow separatrix reconnection, respectively. Zhang *et al.* (2014) studied the substructures of a CBP that consisted of two lobes and showed repeated brightenings or flashes on 2009 August 22–23. The two lobes brightened alternately, and the large-scale overlying coronal loop drifted in the opposite directions during the last two flashes, which is strongly indicative of interchange reconnections. The double sympathetic events to the east of the CBP with time delay of  $< 9$  minutes were further studied by Zhang and Ji (2013). The authors proposed that a likely agent of energy transport from the primary CBP to sympathetic events is a thermal conduction front. However, the mechanism of jet flow could not be excluded. In this article, we present observations of two groups of jets. The first group of six jets occurred during 16:30–19:00 UT on 2014 September 10, which we call J1–J6. All of these jets originated from the same primary CBP, which we call BP1. We show that the jets flowed along closed magnetic loops. We can identify two such loops: one loop connects BP1 with another bright point, which we call BP2; the second loop connects BP1 with a different bright point, which we call BP3. The second group of jets took place during 15:55–15:58 UT at the boundary of AR 11092 on 2010 August 3. The jets originated from the same primary CBP, which we call BP. We could also identify one small-scale loop that connects BP with the AR. Of particular interest are the multiple blobs in the jets. In Section 2 we describe the data analysis. Results of the two groups of jets are presented in Section 3. Discussion and summary are given in Sections 4 and 5.

## 2. Data Analysis

The jets on 2014 September 10 were observed by the *Extreme-Ultraviolet Imager* (EUVI) in the *Sun Earth Connection Coronal and Heliospheric Investigation* (SECCHI; Howard *et al.*, 2008) package of the *Solar TERrestrial RELations Observatory* (STEREO; Kaiser, 2005). The *Ahead* satellite (hereafter STA) and the *Behind* satellite (hereafter STB) had separation angles of  $\sim 167^\circ$  and  $\sim 161^\circ$  with respect to the Sun–Earth direction. Data from STA were not available at the time of this set of jets, and these jets occurred on the far side of the Sun from SDO. Therefore, we only observed this set of jets with STB. The four filters of EUVI (171, 195, 284, and 304 Å) have a spatial resolution of  $3.2''$  and cadences of 75 s, 300 s, 300 s, and 150 s, respectively. Hence, we mainly used the full-disk 171 Å and 304 Å images. Calibration of the EUVI data was performed using the standard Solar Software (SSW) program *secchi\_prep.pro*. The deviation of STB north–south direction from the solar rotation axis was corrected for. Since the intensity contrast between the jets and background quiet region was very low, we also made base-difference and running-difference images to show the jets and CBPs more clearly. The 171 Å and 304 Å images at 17:20:12 UT and 17:19:12 UT before the onset of jets are taken as the base images.

The jets on 2010 August 3 were observed by SDO/AIA in six of the EUV filters (94, 131, 171, 193, 211, and 335 Å). Compared with STEREO/EUVI, AIA has a much higher spatial resolution ( $1.2''$ ) and time cadence (12 s). The full-disk level\_1 data were calibrated using the standard SSW program *aia\_prep.pro*. The images in various filters were carefully co-aligned with an accuracy of  $0.6''$ . We performed DEM inversion and studied the temperature properties of the blobs in the jets. The intensity of an optically thin line  $i$  is

$$I_i = \int_{T_{\min}}^{T_{\max}} \text{DEM}(T) \times R_i(T) dT, \quad (1)$$

where  $\log T_{\min} = 5.5$  and  $\log T_{\max} = 7.5$  stand for the lowest and highest temperatures for the integral and  $R_i(T)$  represents the temperature response function of line  $i$ . The definition

**Table 1** Description of the observational parameters.

Date	Time (UT)	Instrument	$\lambda$ (Å)	Cadence (second)	Pixel size (arcsec)	Location
2014/09/10	16:30–19:00	STB/EUVI	171	75	1.6	backside
2014/09/10	16:30–19:00	STB/EUVI	304	150	1.6	backside
2014/09/10	16:30–19:00	STB/EUVI	195, 284	300	1.6	backside
2010/08/03	15:55–15:58	SDO/AIA	94–335	12	0.6	AR 11092

and expression of DEM is

$$\text{DEM}(T) = \frac{d\text{EM}}{dT} = n_e^2 \frac{dh}{dT}, \quad (2)$$

where EM stands for the total column emission measure along the line of sight (LOS)

$$\text{EM} = \int_{T_{\min}}^{T_{\max}} \text{DEM}(T) dT = \int n_e^2 dh. \quad (3)$$

Here,  $n_e$  denotes the electron number density. The DEM-weighted average electron temperature along the LOS is

$$T_e = \frac{\int_{T_{\min}}^{T_{\max}} \text{DEM} \times T \times dT}{\int_{T_{\min}}^{T_{\max}} \text{DEM} dT} = \frac{\int_{T_{\min}}^{T_{\max}} \text{DEM} \times T \times dT}{\text{EM}}. \quad (4)$$

Since the jets occurred at the AR boundary, background subtraction had to be conducted. We took the EUV images at  $\sim 15:52$  UT before the jets as base images and derived the base-difference images during the jets. We carried out DEM reconstructions using the base-difference intensities of the blobs in the six filters and the same program as in Zhang and Ji (2014b). To evaluate the uncertainties of the reconstructed DEM curves, 100 Monte Carlo (MC) simulations were conducted for each inversion (Cheng *et al.*, 2012). The observational parameters are summarized in Table 1.

### 3. Results

#### 3.1. Jets on 2014 September 10

Figure 1 shows the EUV images observed in 171 Å, 195 Å, 284 Å, and 304 Å when J2 took place. It is clear that the weak, slim jet was ejected in the northeast direction from BP1 located at  $(-130'', 260'')$  in a quiet-Sun region. As a result of the impulsive nature of the jet and the low cadence of 284 Å, the jet was absent from 284 Å with a formation temperature of  $\sim 2$  MK. Nevertheless, bright coronal loops are evident in 284 Å. The rectangular dashed box with size of  $160'' \times 120''$  in panel (d) represents the field of view (FOV) of the panels in Figures 2–7.

Figure 2 shows eight snapshots of the 171 Å running-difference images during J1 and J2. With increasing brightness of BP1, the jet (J1) was ejected outward from BP1 in the northeast direction (see panel (b)). After  $\sim 17:36$  UT, J2 occurred at the same place. Interestingly, we find bright and compact features in J2. Four and five such features are identified

**Figure 1** (a)–(d) EUV images taken by STB/EUVI in 171 Å, 195 Å, 284 Å, and 304 Å around 17:39 UT on 2014 September 10. The homologous jets originate from BP1. The white arrows point at the slim and weak jet (J2) in panels (a), (b), and (d). The larger dashed box in panel (d) shows the FOV (160'' × 120'') of Figures 2–7.

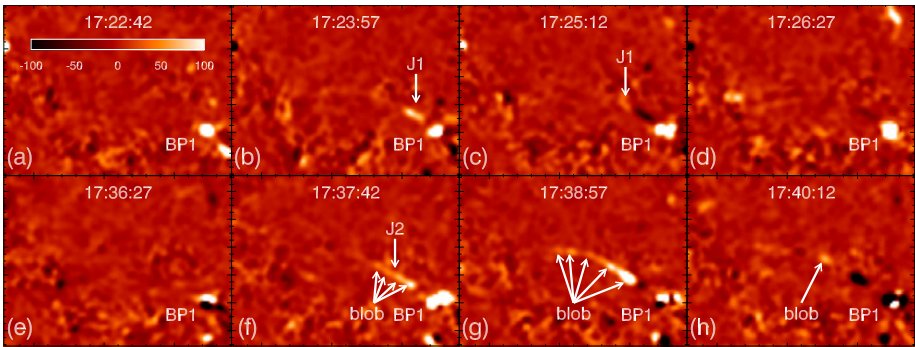
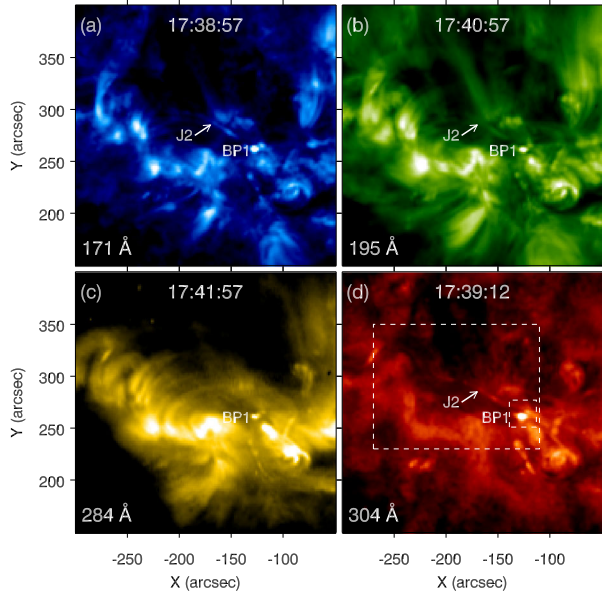


**Figure 2** (a)–(h) Running-difference images in 171 Å during J1 and J2. In panels (b)–(c), the white arrows point at J1. In panels (f)–(h), the multiple white arrows point at the bright and compact blobs in J2.

by eye at 17:37:42 UT and 17:38:57 UT, as indicated by the white arrows. In view of the extraordinary resemblance to the blobs reported by Zhang and Ji (2014b), we also consider the features as blobs. The discrete, circular or elliptical blobs with sizes of 4.5–7.5 Mm moved along the jets like sliding pearls along a necklace.

The 304 Å running-difference images during J1 and J2 are displayed in Figure 3. As a result of the short lifetime of J1 and the low cadence of 304 Å, J1 was hardly identified. However, multiple blobs are distinct in 304 Å at 17:39:12 UT, as indicated by the white arrows, which is consistent with those in Figure 2(g).

Figure 4 shows the 171 Å base-difference images during J3 and J4. Starting from ~ 17:47 UT, the jet (J3) propagated in the northeast direction from BP1 and terminated at BP2 about 9 minutes later (see panel (j)). BP2 is located at (−237'', 314''), which is ~ 120'' away from BP1. Afterward, the brightness of BP2 gradually decreased until it disappeared. Like J2, J3 is not coherent. It consists of blobs propagating along the jet, as indicated by the yellow

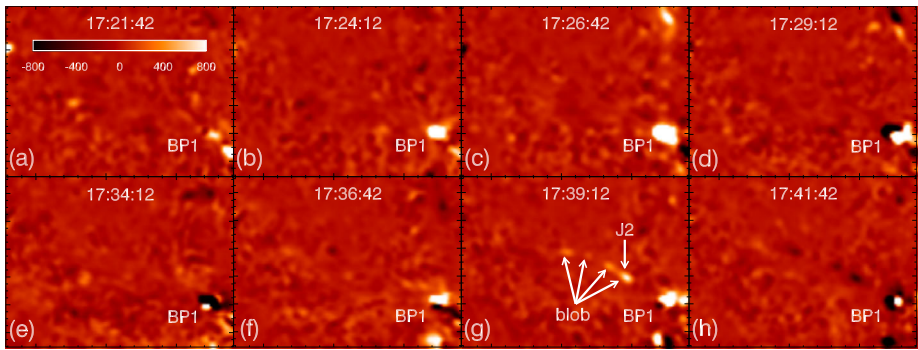


**Figure 3** (a)–(h) Running-difference images in 304 Å during J1 and J2. In panel (g), the multiple white arrows point at the bright and compact blobs in J2.

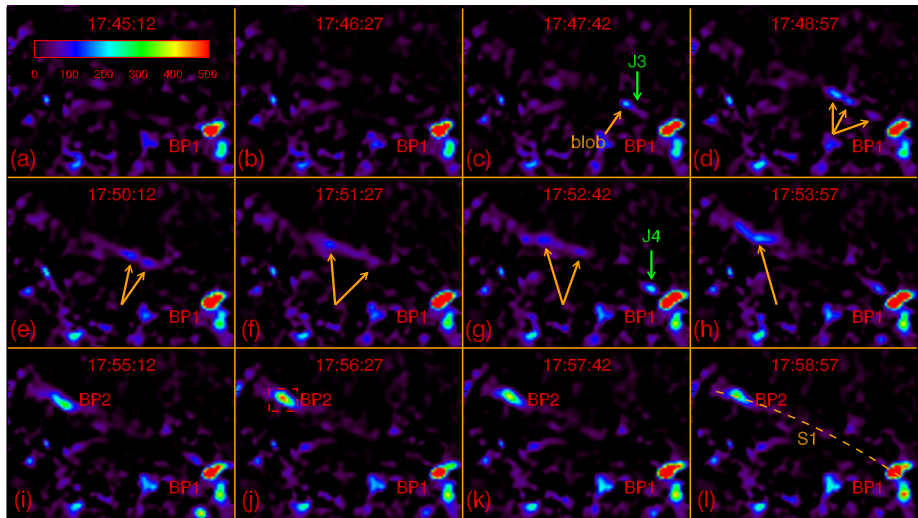


**Figure 4** (a)–(l) Base-difference images in 171 Å during J3 and J4. In panels (c)–(h), the yellow arrows point at the blobs in J3. In panel (g), the green arrow points at J4. The yellow dashed slice labeled S1 in panel (l) is used to study the temporal evolutions of the jets and the first sympathetic event (BP2). The length of S1 is 149.5''.

arrows in panels (c)–(h). The sizes of the blobs range from 6.5 Mm to 8.0 Mm. The short J4 appeared at ~ 17:52 UT and disappeared at ~ 17:57 UT. The 304 Å base-difference images during J3 and J4 are presented in Figure 5. Similar to Figure 4, the blobs propagated along J3 and stopped at BP2, as indicated by the yellow arrows in panels (c)–(e).

Figure 6 shows the 171 Å base-difference images during J5 and J6. The short jet (J5) was ejected from BP1 in the northeast direction after ~ 18:06 UT, as indicated by the green arrows in panel (b). After ~ 18:12 UT, J6 spurted from BP1 in the same direction and propagated to BP3, which is located at (−230'', 280'') and is ~ 105'' away from BP1. Afterward, the intensity of BP3 gradually decreased and finally disappeared. We note that the trajectory of J6 is close to that of J3 in the initial phase, but different at the ending phase, although both J3 and J6 produced remote brightening at the other end of

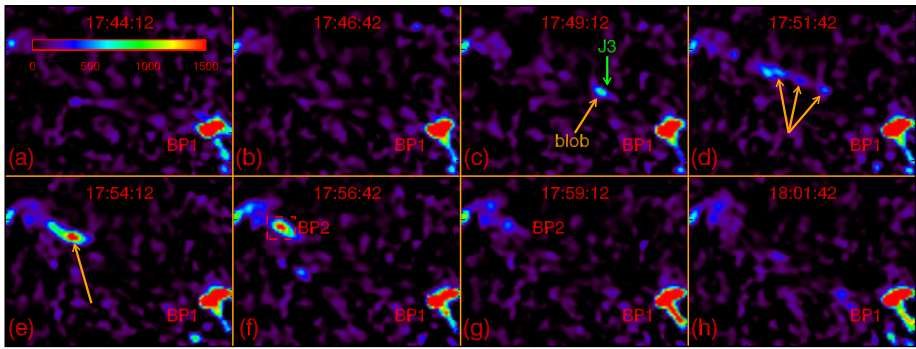


**Figure 5** (a)–(h) Base-difference images in 304 Å during J3 and J4. In panels (c)–(e), the yellow arrows point at the blobs in J3.

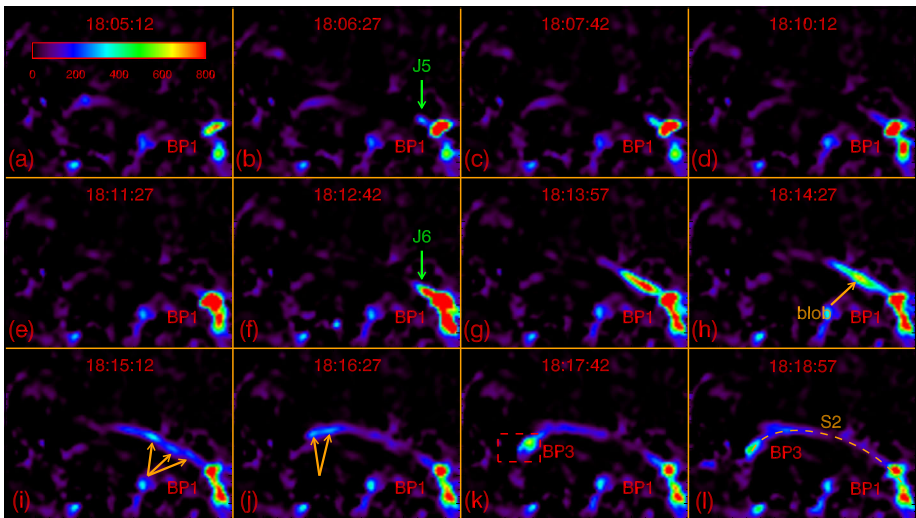


**Figure 6** (a)–(l) Base-difference images in 171 Å during J5 and J6. In panel (b), the green arrow points at J5. In panels (h)–(j), the yellow arrows point at the blobs in J6, which is indicated by the green arrow in panel (f). The yellow dashed slice labeled S2 in panel (l) is used to study the temporal evolutions of the jets and the second sympathetic event (BP3). The length of S2 is 123.2''.

large-scale coronal loops. Likewise, multiple blobs are recognized in J6 by eye, as indicated by the yellow arrows in panels (h)–(j). Figure 7 shows the 304 Å base-difference images during J5 and J6. J5 is not obvious in 304 Å because of the low cadence. However, J6 is very clear with blobs at 18:14:12 UT and 18:16:42 UT. Table 2 summarizes the information on the homologous jets, including the wavelengths of observation ( $\lambda$ ), start and end times in 171 Å, lifetimes, apparent lengths, apparent velocities, and the related CBP.

To investigate the temporal evolution of the jets, we extracted two curved slices. The first slice (S1) is superposed in Figure 4(l) with a yellow dashed line that passes through BP1 and BP2. The second slice (S2) is superposed in Figure 6(l) with a yellow dashed line that passes through BP1 and BP3. The time-slice diagrams of S1 and S2 in 171 Å and 304 Å



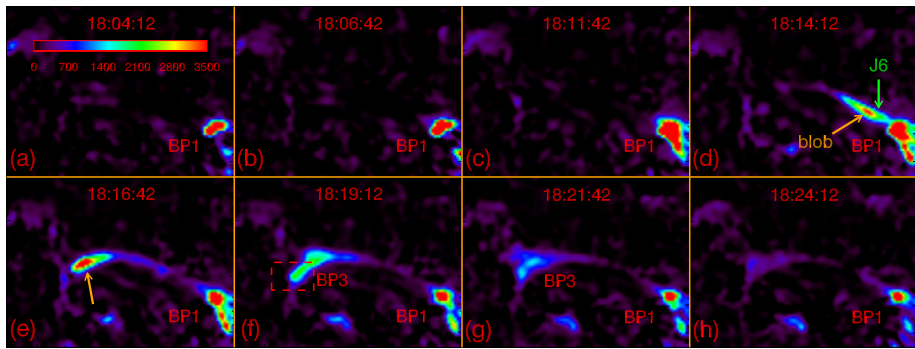


**Figure 7** (a)–(h) Base-difference images in 304 Å during J5 and J6. In panels (d)–(e), the yellow arrows point at the blobs in J6.

**Table 2** Information on the homologous coronal jets (J1–J6) on 2014 September 10.

Jet	$\lambda$ (Å)	$t_{\text{start}}$ (UT)	$t_{\text{end}}$ (UT)	Lifetime (s)	Length (arcsec)	Velocity ( $\text{km s}^{-1}$ )	CBP
J1	171	17:23:57	17:26:27	$150 \pm 75$	$26.2 \pm 1.6$	$145 \pm 15$	–
J2	171, 304	17:37:42	17:41:27	$225 \pm 75$	$50.7 \pm 1.6$	$203 \pm 8$	–
J3	171, 304	17:47:42	17:53:57	$375 \pm 75$	$124.6 \pm 1.6$	$381 \pm 18$	BP2
J4	171	17:52:42	17:56:27	$225 \pm 75$	$28.8 \pm 1.6$	$175 \pm 13$	–
J5	171	18:06:27	18:11:27	$300 \pm 75$	$16.7 \pm 1.6$	$222 \pm 34$	–
J6	171, 304	18:12:42	18:18:57	$375 \pm 75$	$108.2 \pm 1.6$	$249 \pm 3$	BP3

are shown in Figure 8. The  $x$ - and  $y$ -axes denote the distances from the left endpoints of the slices and the time (UT) in each panel. In panel (a), the homologous jets (J1–J6) are represented by the bright and inclined structures whose inverse slopes indicate their apparent speeds, which are  $145 \pm 15$ ,  $203 \pm 8$ ,  $381 \pm 18$ ,  $175 \pm 13$ ,  $222 \pm 34$ , and  $224 \pm 7 \text{ km s}^{-1}$ , respectively. It is clear that J3 propagates along S1 and reaches the left endpoint of S1, producing the sympathetic CBP, *i.e.*, BP2 around 17:56 UT. In panel (b), only J2, J3, and J6, whose greatest apparent lengths are longer than J1, J4, and J5, are evident. J6 propagates along S2 and reaches the left endpoint of S2, producing the sympathetic CBP, *i.e.*, BP3 around 18:17 UT. The more accurate apparent speed of J6 derived from panel (b) is  $249 \pm 3 \text{ km s}^{-1}$ . Owing to the low cadence of the 304 Å filter, only some of the jets (J2, J3, and J6) are clearly identified (see panels (c)–(d)). The intervals of the recurrent jets range from 5 to 15 minutes.

In Figure 9 we plot the light curves of BP1, BP2, and BP3 in 171 Å and 304 Å with solid, dashed, and dotted lines, respectively. The light curves are calculated to be the average intensities of BP1, BP2, and BP3 in the small box of Figure 1(d), Figure 4(j), and Figure 6(k). During 17:20–18:30 UT, BP1 experiences several flashes, whose peak times (p1–p6) are labeled with the red dashed line. The last flash is the strongest, which is similar to the case of CBP on 2009 August 22–23 observed in SXR (Zhang *et al.*, 2014). The intensity of BP2 increases slowly from 17:40 UT and rapidly from  $\sim 17:50$  UT before reaching its maximum at  $\sim 17:56:30$  UT. Afterward, they decrease to the initial levels by  $\sim 18:10$  UT. The lifetime of BP2 is  $27.5 \pm 2.5$  minutes. Since BP1 reaches the third peak (p3) at  $\sim 17:52:30$  UT,

**Figure 8** Time-slice diagrams of S1 (left panels) and S2 (right panels) in 171 Å (top panels) and 304 Å (bottom panels). The homologous jets (J1–J6) are bright and inclined structures whose inverse slopes indicate the apparent velocities of the jets marked by the white arrows. The distances between the vertical dashed lines represent the distances between BP1 and BP2 (BP3) in the upper panels.

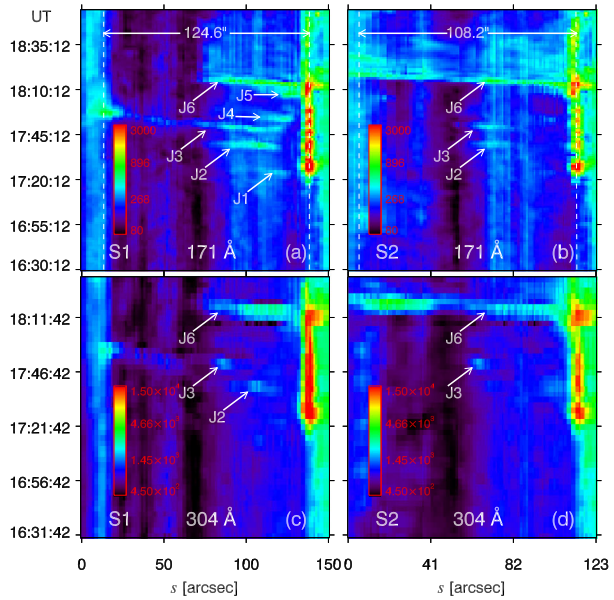
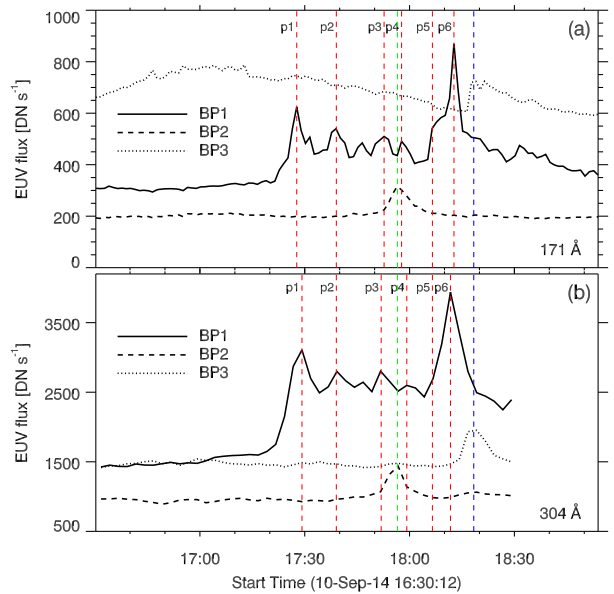


**Figure 9** (a)–(b) Light curves of BP1 (solid lines), BP2 (dashed lines), and BP3 (dotted lines) in 171 Å and 304 Å, respectively. The light curves are calculated to be the average intensities of BP1, BP2, and BP3 within the small dashed boxes of Figure 1(d), Figure 4(j), and Figure 6(k), respectively. The vertical red, green, and blue lines represent the peak times of BP1 (p1–p6), BP2, and BP3, respectively.



the time delay between BP2 and BP1 is  $240 \pm 75$  s. The intensity of BP3 increases from  $\sim 18:13:30$  UT and reach its maximum at  $\sim 18:17:30$  UT before declining to the initial level by  $\sim 18:43$  UT. The lifetime of BP3 is  $27.4 \pm 2.5$  minutes. Considering that the peak time of the sixth flash of BP1, *i.e.* p6, is  $\sim 18:12:30$  UT, the time delay between BP3 and BP1 is  $300 \pm 75$  s.

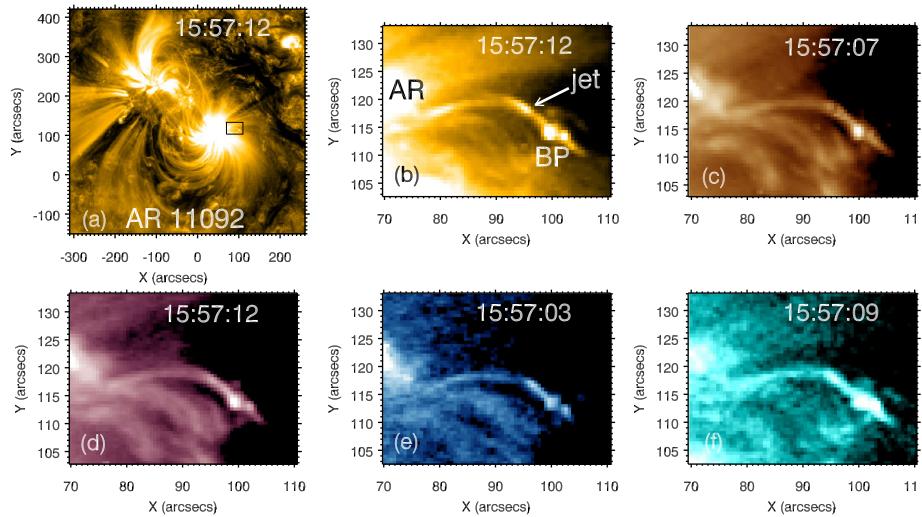


**Figure 10** (a) EUV image of the AR 11092 at 15:57:12 UT on 2010 August 3 observed by SDO/AIA in 171 Å. (b)–(f) Amplified EUV images of the jets and BP originating at the AR boundary observed in five of the AIA filters, *i.e.*, 171 Å, 193 Å, 211 Å, 335 Å, and 131 Å. The FOV of these images is indicated by the small black rectangular box in panel (a).

### 3.2. Jets on 2010 August 3

In Figure 10, the 171 Å image of the AR 11092 at 15:57:12 UT is shown in panel (a). The jets were located at the western AR boundary in the black rectangular box ( $40'' \times 30''$ ). In panels (b)–(f), we plot the EUV images of the jets observed in 171, 193, 211, 335, and 131 Å around 15:57 UT. It is clear that the jets originated from the bright point (BP) and propagated in the northeast direction along the small-scale closed loop that is  $\sim 28$  Mm in length before flowing into the AR. The bright jets with enhanced emission measure were observed in all the EUV filters, although we show the jets only in five filters.

Compared with the first group of jets, the second group was short-lived. The whole evolution is displayed in the 171 Å base-difference images of Figure 11. The jet started at  $\sim 15:55$  UT and moved in the northeast direction, with the intensity of BP at its base increasing. Interestingly, the jet was not coherent and smooth. Instead, there were bright and compact structures similar to the blobs in the jets observed by EUVI. In panels (f)–(o), we highlight the blobs with black circles that are  $2.4''$  in diameter. The blob appeared at  $\sim 15:56:00$  UT (panel (f)) and propagated along the closed loop for  $\leq 12$  s. A new blob appeared at 15:56:24 UT (panel (h)) and lasted until  $\sim 15:56:48$  UT (panel (j)). The velocity of this blob is calculated to be  $238 \text{ km s}^{-1}$ . Then, another blob appeared close to the BP and flowed forward until  $\sim 15:57:12$  UT (panel (l)). Afterward, three blobs were identified during the late phase of the evolution. As the brightness of the BP decreased slowly, the jet faded and disappeared. Since the jets flowed into the AR, sympathetic CBPs were not observed at the remote footpoint of the loop, perhaps due to an increased brightness level there.

The blobs were visible not only in 171 Å, but also in other wavelengths. In Figure 12 we show base-difference images in 94, 335, 211, 193, and 131 Å from the top to bottom row, with the blobs indicated by white arrows. In each column, the observing times are very similar, but not co-temporal. As in 171 Å, the blobs are bright and compact features moving

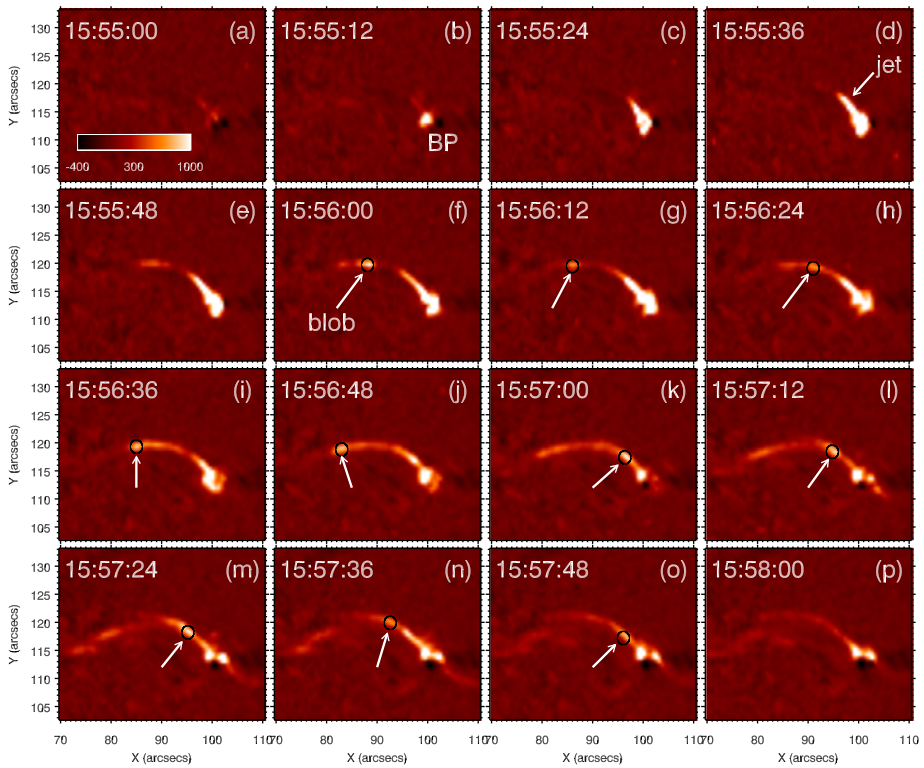


**Figure 11** (a)–(p) Base-difference  $171 \text{ \AA}$  images of the jets and BP. In panels (f)–(o), the white arrows point at the black encircled blobs.

along the closed loop. It should be noted that a blob is not always evident and striking in all the wavelengths. The presence of blobs in multiple wavelengths indicates their multithermal nature.

To study the temperature properties of the blobs, we performed DEM reconstructions as described in Section 2. Figure 13 shows the DEM profiles of the ten blobs indicated by the arrows in Figure 11(f)–(o). The red solid lines stand for the best-fit DEM curves from the observed values, while the black dashed lines represent the reconstructed curves from the 100 MC simulations. Except for the ninth blob, all the profiles have similar shapes in the range of  $5.5 < \log T[\text{K}] < 7.5$ , with most of the emissions coming from the low-temperature plasma. The uncertainties of the DEM curves are smallest in the range of  $5.8 < \log T[\text{K}] < 6.5$  and increase significantly toward the low- and high-temperature ends. The calculated EM of the blobs ranges from  $5 \times 10^{26} \text{ cm}^{-5}$  to  $1.4 \times 10^{27} \text{ cm}^{-5}$ . Assuming that the LOS depths of the blobs are equal to their widths, *i.e.*,  $2.4''$ , the electron number densities of the blobs are estimated to be  $(1.7\text{--}2.8) \times 10^9 \text{ cm}^{-3}$ . The calculated  $T_e$  of the blobs ranges from 1.8 MK to 3.1 MK except for the ninth blob, and most of them are between 2 MK and 3 MK.

## 4. Discussion

So far, only a few studies were made of plasmoids or blobs in coronal jets. Using the multi-wavelength observations of AIA on 2011 July 22, Zhang and Ji (2014b) studied such recur-

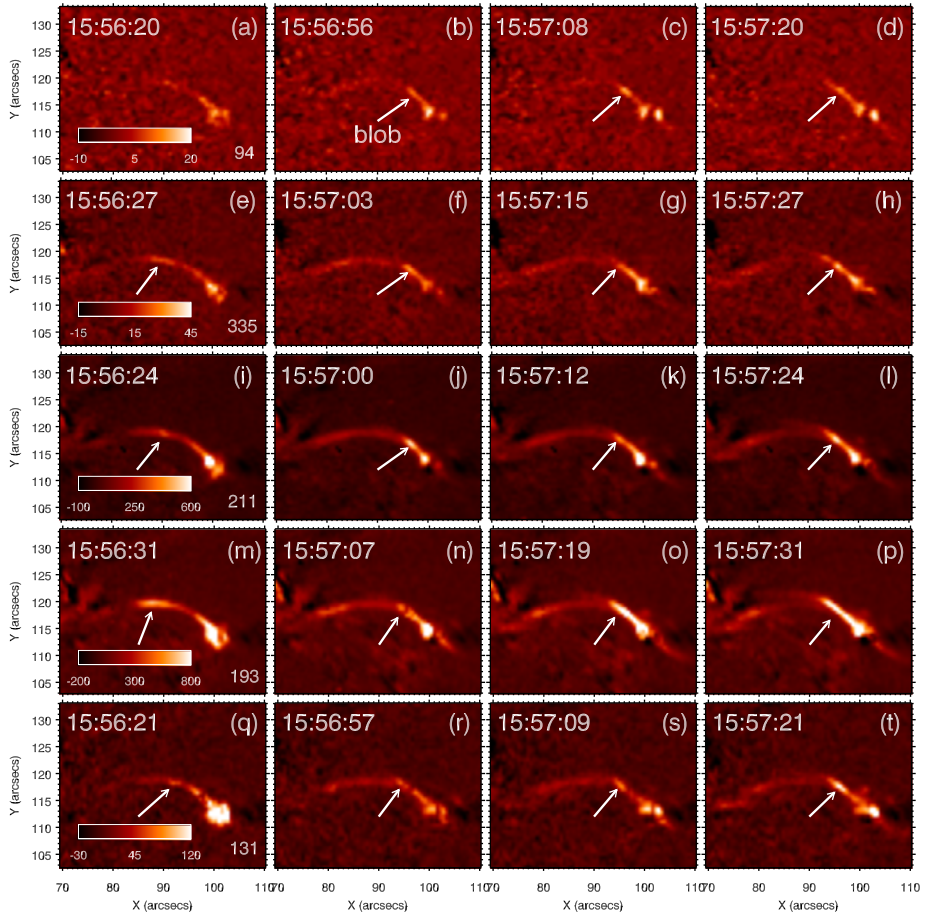


**Figure 12** From top to bottom row: Base-difference EUV images of the jets and BP in 94, 335, 211, 193, and 131 Å. The white arrows point at the blobs.

**Table 3** Comparison of the parameters of the blobs.

Date	Instr.	Size (Mm)	Lifetime (second)	Velocity (km s <sup>-1</sup> )	$T_e$ (MK)	$n_e$ (10 <sup>9</sup> cm <sup>-3</sup> )	Mag. field
2011/07/22 <sup>a</sup>	AIA	~ 3	24–60	120–450	0.5–4.0	1.5–3.5	open
2010/08/03	AIA	~ 1.7	24 ± 12	~ 238	1.8–3.1	1.7–2.8	closed
2014/09/10	EUVI	4.5–9.0	–	140–380	–	–	closed

<sup>a</sup>Event studied by Zhang and Ji (2014b).

ring blobs. In this article, we provided additional evidence of multiple recurring blobs in the homologous jets. The first group was observed by STB/EUVI, the second group by AIA. In Table 3 we compare the parameters of the blobs. On one hand, the measured sizes of the blobs observed by EUVI are 2–5 times larger than those observed by AIA. Considering that

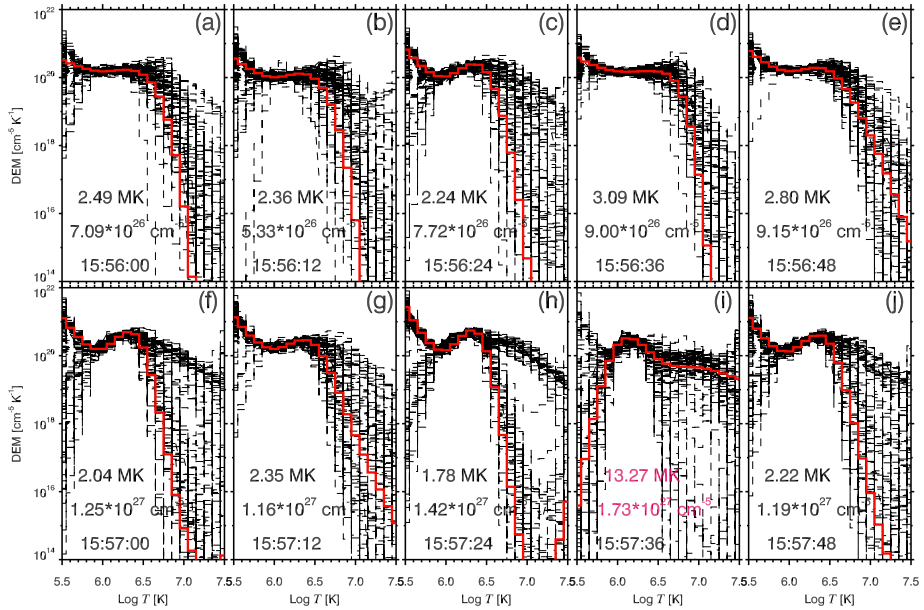


**Figure 13** (a)–(j) DEM profiles of the blobs indicated by the arrows in Figure 11(f)–(o). The red solid lines stand for the best-fit DEM curves from the observed values. The black dashed lines represent the reconstructed curves from the 100 MC simulations. The corresponding  $T_e$  (MK) and EM ( $\text{cm}^{-5}$ ) are displayed.

the resolution of EUVI is lower than that of AIA, the blobs observed by EUVI may not be fully resolved and the obtained blob sizes with large uncertainties may not be reliable. On the other hand, both the sizes of blobs and CBP at its base on 2010 August 3 are about twice as small as those for the event on 2011 July 22. In chromospheric anemone jets, the sizes of blobs (0.3–1.5 Mm) and the base loops are even smaller (Singh *et al.*, 2012), implying that the same process may exist at different scales in the solar atmosphere. The lifetimes of the blobs in coronal jets observed by AIA range from 12 s to 60 s, which is similar to the typical value of chromospheric blobs (Singh *et al.*, 2012). The apparent speeds of the blobs are on the order of the coronal Alfvén speed, *i.e.*, hundreds of  $\text{km s}^{-1}$ , are consistent in the FOVs of AIA and EUVI. For the events observed by AIA, the DEM-weighted average temperatures of the blobs agree with each other, suggesting that the method of inversion we used is correct. In addition, the DEM profiles are similar. Possible causes of the problematic inversion result for the ninth blob in Figure 13(i) and the large uncertainties of all the profiles at the low- and high-temperature ends are as follows. i) The intensities of the blobs are not high enough, *i.e.*, the signal-to-noise ratios are not sufficient. ii) The observing times of the six filters used for inversion are not exactly the same. Therefore, the positions of the blobs may be misplaced more or less even though we took the AIA images at the nearest times. Assuming that the velocity of a blob is  $200 \text{ km s}^{-1}$ , the largest displacement of the blob in the EUV images is 1.6 Mm, which is close to the size of the blobs. In this regard, multi-wavelength observations with much higher cadence are required in the future. The rough estimates of the number density in blobs are also in the same range, assuming that the LOS depth equals the width or size. Although jets along open magnetic fields are more common, there are a few reports on the observations of coronal jets along closed loops (Zhang and Ji, 2013; Zhang *et al.*, 2014). The blobs in jets associated with both open and closed magnetic

fields indicate that this type of bright and compact structure is ubiquitous. According to previous theoretical and numerical studies (*e.g.*, Furth, Killeen, and Rosenbluth, 1963; Drake *et al.*, 2006; Bárta, Vršnak, and Karlický, 2008), the blobs are most probably plasmoids created by the tearing-mode instability of the current sheet where magnetic reconnection takes place.

Sympathetic phenomena are common in the solar atmosphere because of the complexity and interconnection of the magnetic field lines. Sympathetic flares have been extensively reported and investigated in the past decades (*e.g.* Lang and Willson, 1989; Hanaoka, 1996; Masson *et al.*, 2009; Wang and Liu, 2012; Deng *et al.*, 2013; Sun *et al.*, 2013; Yang, Zhang, and Xiang, 2014; Liu *et al.*, 2015a). Possible agents of energy transported from the source region of energy release to the remote footpoints are nonthermal electrons (Tang and Moore, 1982; Nakajima *et al.*, 1985; Martin and Svestka, 1988), a thermal conduction front (Rust, Simnett, and Smith, 1985; Bastian and Gary, 1992), shock waves (Machado *et al.*, 1988), and reconnection outflows (Hanaoka, 1996; Nishio *et al.*, 1997). In a cartoon model, Machado *et al.* (1988) compared the velocities of different agents, among which nonthermal electrons have the fastest speed (about one-third of the speed of light). The electrons are followed by thermal conduction, plasma shock, and evaporated material. Therefore, the time delays between the start and peak times of the main and sympathetic events are different for different energy agents. In the rare case of double sympathetic events studied by Zhang and Ji (2013), the time delays between BP1 and BP2 (BP3) are shorter than nine minutes. The authors proposed that thermal conduction plays a role in the energy transport. Nevertheless, it is difficult to distinguish thermal conduction and jet flow in observations. In this study, the jets (J3 and J6) reached the remote footpoints of the pre-existing large-scale coronal loops and produced sympathetic CBPs (BP2 and BP3) observed in 171 Å and 304 Å. The pre-existing loops may have a lower electron number density and emission measure so that they are not clearly revealed in 284 Å before the jets. The time delays between BP1 and BP2 (BP3) are approximately  $240 \pm 75$  s ( $300 \pm 75$  s). Considering that the lengths of the coronal loops between BP1 and BP2 (BP3) are  $\sim 124.6''$  and  $\sim 108.2''$ , as indicated in the upper panels of Figure 8, the velocities of the energy transport are estimated to be  $376.4_{-90}^{+171}$  and  $261.5_{-52}^{+87}$  km s<sup>-1</sup>, which are consistent with the apparent velocities of J3 and J6. On one hand, the transit times of the nonthermal electrons from BP1 to BP2 and BP3 are  $\sim 1$  s, which are significantly shorter than the observed time delays. On the other hand, thermal conduction timescales of the coronal loops are  $\tau_c = 4 \times 10^{-10} n_e L^2 T_e^{-5/2}$ , where  $n_e$ ,  $T_e$ , and  $L$  represent the number density of the jets, temperature of the jets, and length of the loops (Cargill, 1994). Assuming that  $n_e = 10^9$  cm<sup>-3</sup> and  $T_e = 2$  MK, the values of  $\tau_c$  between BP1 and BP2 (BP3) are estimated to be  $\sim 5770$  s ( $\sim 4351$  s), which are much longer than the observed values. If the thermal conduction front really plays a dominant role, the temperatures of BP1 and jets should be 6–7 MK in the case of  $n_e = 10^9$  cm<sup>-3</sup>, which seems to be unlikely because the response of the 171 Å filter decreases from the maximum value by 3–4 orders of magnitude at such a high temperature. Interestingly, we identified multiple and recurring blobs in the jet flows, which is in favor of the jet flow and not of the thermal conduction front to be the most probable energy propagation agent because the conduction front should result in smooth and not clumpy brightenings.

## 5. Summary

We reported our multiwavelength observations of two groups of homologous jets. The first was observed by STB/EUVI on 2014 September 10, the second was observed by SDO/AIA on 2010 August 3. The main results are summarized as follows:

- i) The first group of recurring jets originated from BP1 and propagated in the northeast direction along large-scale closed coronal loops during the six eruptions (J1–J6). The intervals between the recurring jets ranged from 5 to 15 minutes. Two of the jets (J3 and J6) produced sympathetic CBPs (BP2 and BP3) after reaching the remote footpoints of the loops. The peak times of the sympathetic CBPs were delayed by 240–300 s relative to BP1.
- ii) The jets were not coherent. Instead, they were composed of bright and compact structures, *i.e.*, blobs. The sizes and apparent velocities of the blobs were 4.5–9 Mm and 140–380 km s<sup>-1</sup>, respectively. The existence of multiple blobs in the jets suggests that the sympathetic CBPs are caused by jet flows and not by a thermal conduction front.
- iii) The second group of jets originated from a BP at the boundary of AR 11092 and propagated in the northeast direction along a small-scale closed coronal loop. Sympathetic CBPs were not observed at the remote footpoint of the loop (although it is possible that the remote footpoint was hidden in the glare of the AR). Like in the first group, we also identified blobs in the jets. The sizes and apparent velocities of the blobs are  $\sim 1.7$  Mm and  $\sim 238$  km s<sup>-1</sup>, respectively.
- iv) Using the AIA base-difference EUV images, we performed DEM inversions and derived the DEM profiles of the blobs. The blobs are multithermal with temperatures of 1.8–3.1 MK. The estimated number density of the blobs are  $(1.7\text{--}2.8) \times 10^9$  cm<sup>-3</sup>. Additional case studies with high resolution and cadence are expected in the future. Multi-dimensional MHD simulations are underway to investigate the nature of plasmoids and mechanism of sympathetic CBPs.

**Acknowledgements** The authors acknowledge the referee for detailed comments and valuable suggestions. We are also grateful to E. Pariat, L. Ni, T. Li, Y.H. Yan, S.L. Ma, P.F. Wyper, C.R. DeVore, and P. Syntelis for constructive discussions. STEREO/SECCHI data are provided by a consortium of US, UK, Germany, Belgium, and France. SDO is a mission of NASA's Living With a Star Program. AIA data are courtesy of the NASA/SDO science teams. Q.M.Z. is supported by NSFC No. 11303101, 11333009, 11473071, and 11573072. H.S. Ji is supported by the Strategic Priority Research Program—The Emergence of Cosmological Structures of the CAS, Grant No. XDB09000000. Yingna Su is supported by NSFC 11473071, Youth Fund of Jiangsu BK20141043, and the One Hundred Talent Program of Chinese Academy of Sciences.

## References

- Alipour, N., Safari, H.: 2015, *Astrophys. J.* **807**, 175. DOI.
- Archontis, V., Hood, A.W.: 2013, *Astrophys. J. Lett.* **769**, LL21. DOI.
- Asai, A., Yokoyama, T., Shimojo, M., Shibata, K.: 2004, *Astrophys. J. Lett.* **605**, L77. DOI.
- Bárta, M., Vršnak, B., Karlický, M.: 2008, *Astron. Astrophys.* **477**, 649. DOI.
- Bastian, T.S., Gary, D.E.: 1992, *Solar Phys.* **139**, 357. DOI.
- Cargill, P.J.: 1994, *Astrophys. J.* **422**, 381. DOI.
- Chae, J., Qiu, J., Wang, H., Goode, P.R.: 1999, *Astrophys. J. Lett.* **513**, L75. DOI.
- Chandra, R., Gupta, G.R., Mulay, S., Tripathi, D.: 2015, *Mon. Not. Roy. Astron. Soc.* **446**, 3741. DOI.
- Chen, H.D., Zhang, J., Ma, S.L.: 2012, *Res. Astron. Astrophys.* **12**, 573. DOI.
- Chen, J., Su, J., Yin, Z., Priya, T.G., Zhang, H., Liu, J., *et al.*: 2015, *Astrophys. J.* **815**, 71. DOI.
- Cheng, X., Zhang, J., Saar, S.H., Ding, M.D.: 2012, *Astrophys. J.* **761**, 62. DOI.
- Chifor, C., Isobe, H., Mason, H.E., Hannah, I.G., Young, P.R., Del Zanna, G., *et al.*: 2008, *Astron. Astrophys.* **491**, 279. DOI.
- Cirtain, J.W., Golub, L., Lundquist, L., van Ballegooijen, A., Savcheva, A., Shimojo, M., *et al.*: 2007, *Science* **318**, 1580. DOI.
- Culhane, L., Harra, L.K., Baker, D., van Driel-Gesztelyi, L., Sun, J., Doschek, G.A., *et al.*: 2007, *Publ. Astron. Soc. Japan* **59**, 751. DOI.
- Deng, N., Tritschler, A., Jing, J., Chen, X., Liu, C., Reardon, K., *et al.*: 2013, *Astrophys. J.* **769**, 112. DOI.
- Drake, J.F., Swisdak, M., Che, H., Shay, M.A.: 2006, *Nature* **443**, 553. DOI.



- Fang, F., Fan, Y., McIntosh, S.W.: 2014, *Astrophys. J. Lett.* **789**, LL19. DOI.
- Furth, H.P., Killeen, J., Rosenbluth, M.N.: 1963, *Phys. Fluids* **6**, 459. DOI.
- Golub, L., Krieger, A.S., Silk, J.K., Timothy, A.F., Vaiana, G.S.: 1974, *Astrophys. J. Lett.* **189**, L93. DOI.
- Guo, Y., Démoulin, P., Schmieder, B., Ding, M.D., Vargas Domínguez, S., Liu, Y.: 2013, *Astron. Astrophys.* **555**, AA19. DOI.
- Habbal, S.R., Withbroe, G.L.: 1981, *Solar Phys.* **69**, 77. DOI.
- Hanaoka, Y.: 1996, *Solar Phys.* **165**, 275. DOI.
- Heyvaerts, J., Priest, E.R., Rust, D.M.: 1977, *Astrophys. J.* **216**, 123. DOI.
- Hong, J.C., Jiang, Y.C., Yang, J.Y., Zheng, R.S., Bi, Y., Li, H.D., et al.: 2013, *Res. Astron. Astrophys.* **13**, 253. DOI.
- Hong, J., Jiang, Y., Yang, J., Bi, Y., Li, H., Yang, B., et al.: 2014, *Astrophys. J.* **796**, 73. DOI.
- Howard, R.A., Moses, J.D., Vourlidas, A., Newmark, J.S., Socker, D.G., Plunkett, S.P., et al.: 2008, *Space Sci. Rev.* **136**, 67. DOI.
- Innes, D.E., Cameron, R.H., Solanki, S.K.: 2011, *Astron. Astrophys.* **531**, L13. DOI.
- Innes, D.E., Guo, L.J., Huang, Y.M., Bhattacharjee, A.: 2015, *Astrophys. J.* **813**, 86. DOI.
- Jiang, Y., Bi, Y., Yang, J., Li, H., Yang, B., Zheng, R.: 2013, *Astrophys. J.* **775**, 132. DOI.
- Kaiser, M.L.: 2005, *Adv. Space Res.* **36**, 1483. DOI.
- Kariyappa, R., Varghese, B.A.: 2008, *Astron. Astrophys.* **485**, 289. DOI.
- Kariyappa, R., Deluca, E.E., Saar, S.H., Golub, L., Damé, L., Pevtsov, A.A., et al.: 2011, *Astron. Astrophys.* **526**, AA78. DOI.
- Kliem, B., Karlický, M., Benz, A.O.: 2000, *Astron. Astrophys.* **360**, 715.
- Krieger, A.S., Vaiana, G.S., van Speybroeck, L.P.: 1971, *Solar Magn. Fields* **43**, 397.
- Kumar, P., Cho, K.S.: 2013, *Astron. Astrophys.* **557**, AA115. DOI.
- Lang, K.R., Willson, R.F.: 1989, *Astrophys. J. Lett.* **344**, L77. DOI.
- Lemen, J.R., Title, A.M., Akin, D.J., Boerner, P.F., Chou, C., Drake, J.F., et al.: 2012, *Solar Phys.* **275**, 17. DOI.
- Li, H.D., Jiang, Y.C., Yang, J.Y., Bi, Y., Liang, H.F.: 2015, *Astrophys. Space Sci.* **359**, 44. DOI.
- Lim, E.K., Yurchyshyn, V., Park, S.H., Kim, S., Cho, K.S., Kumar, P., et al.: 2016, *Astrophys. J.* **817**, 39. DOI.
- Lin, J.: 2004, *Solar Phys.* **219**, 169. DOI.
- Lin, J., Ko, Y.K., Sui, L., Raymond, J.C., Stenborg, G.A., Jiang, Y., et al.: 2005, *Astrophys. J.* **622**, 1251. DOI.
- Lin, J., Murphy, N.A., Shen, C., Raymond, J.C., Reeves, K.K., Zhong, J., et al.: 2015, *Space Sci. Rev.* **194**, 237. DOI.
- Liu, C., Deng, N., Liu, R., Lee, J., Pariat, E., Wiegmann, T., et al.: 2015a, *Astrophys. J. Lett.* **812**, L19. DOI.
- Liu, J., Wang, Y., Shen, C., Liu, K., Pan, Z., Wang, S.: 2015b, *Astrophys. J.* **813**, 115. DOI.
- Longcope, D.W.: 1998, *Astrophys. J.* **507**, 433. DOI.
- Machado, M.E., Xiao, Y.C., Wu, S.T., Prokakis, T., Dialetis, D.: 1988, *Astrophys. J.* **326**, 451. DOI.
- Mandrini, C.H., Démoulin, P., van Driel-Gesztelyi, L., Schmieder, B., Cauzzi, G., Hofmann, A.: 1996, *Solar Phys.* **168**, 115. DOI.
- Martin, S.F., Svestka, Z.F.: 1988, *Solar Phys.* **116**, 91. DOI.
- Masson, S., Pariat, E., Aulanier, G., Schrijver, C.J.: 2009, *Astrophys. J.* **700**, 559. DOI.
- Moore, R.L., Cirtain, J.W., Sterling, A.C., Falconer, D.A.: 2010, *Astrophys. J.* **720**, 757. DOI.
- Moore, R.L., Sterling, A.C., Falconer, D.A., Robe, D.: 2013, *Astrophys. J.* **769**, 134. DOI.
- Moreno-Insertis, F., Galsgaard, K.: 2013, *Astrophys. J.* **771**, 20. DOI.
- Moreno-Insertis, F., Galsgaard, K., Ugarte-Urra, I.: 2008, *Astrophys. J. Lett.* **673**, L211. DOI.
- Nakajima, H., Dennis, B.R., Hoyng, P., Nelson, G., Kosugi, T., Kai, K.: 1985, *Astrophys. J.* **288**, 806. DOI.
- Ni, L., Kliem, B., Lin, J., Wu, N.: 2015, *Astrophys. J.* **799**, 79. DOI.
- Ning, Z., Guo, Y.: 2014, *Astrophys. J.* **794**, 79. DOI.
- Nishio, M., Yaji, K., Kosugi, T., Nakajima, H., Sakurai, T.: 1997, *Astrophys. J.* **489**, 976.
- Nisticò, G., Zimbardo, G., Patsourakos, S., Bothmer, V., Nakariakov, V.M.: 2015, *Astron. Astrophys.* **583**, A127. DOI.
- Paraschiv, A.R., Bemporad, A., Sterling, A.C.: 2015, *Astron. Astrophys.* **579**, A96. DOI.
- Pariat, E., Antiochos, S.K., DeVore, C.R.: 2009, *Astrophys. J.* **691**, 61. DOI.
- Pariat, E., Antiochos, S.K., DeVore, C.R.: 2010, *Astrophys. J.* **714**, 1762. DOI.
- Priest, E.R., Parnell, C.E., Martin, S.F.: 1994, *Astrophys. J.* **427**, 459. DOI.
- Pucci, S., Poletto, G., Sterling, A.C., Romoli, M.: 2013, *Astrophys. J.* **776**, 16. DOI.
- Rust, D.M., Simnett, G.M., Smith, D.F.: 1985, *Astrophys. J.* **288**, 401. DOI.
- Samanta, T., Banerjee, D., Tian, H.: 2015, *Astrophys. J.* **806**, 172. DOI.
- Santos, J.C., Büchner, J.: 2007, *Astrophys. Space Sci. Trans.* **3**, 29. DOI.

- Schmieder, B., Guo, Y., Moreno-Insertis, F., Aulanier, G., Yelles Chaouche, L., Nishizuka, N., *et al.*: 2013, *Astron. Astrophys.* **559**, A1. [DOI](#).
- Shibata, K., Ishido, Y., Acton, L.W., Strong, K.T., Hirayama, T., Uchida, Y., *et al.*: 1992, *Publ. Astron. Soc. Japan* **44**, L173.
- Shimojo, M., Shibata, K.: 2000, *Astrophys. J.* **542**, 1100. [DOI](#).
- Shimojo, M., Hashimoto, S., Shibata, K., Hirayama, T., Hudson, H.S., Acton, L.W., *et al.*: 1996, *Publ. Astron. Soc. Japan* **48**, 123. [DOI](#).
- Singh, K.A.P., Isobe, H., Nishizuka, N., Nishida, K., Shibata, K.: 2012, *Astrophys. J.* **759**, 33. [DOI](#).
- Sterling, A.C., Moore, R.L., Falconer, D.A., Adams, M.: 2015, *Nature* **523**, 437. [DOI](#).
- Strong, K.T., Harvey, K., Hirayama, T., Nitta, N., Shimizu, T., Tsuneta, S.: 1992, *Publ. Astron. Soc. Japan* **44**, L161.
- Sun, X., Hoeksema, J.T., Liu, Y., Aulanier, G., Su, Y., Hannah, I.G., *et al.*: 2013, *Astrophys. J.* **778**, 139. [DOI](#).
- Takasao, S., Asai, A., Isobe, H., Shibata, K.: 2012, *Astrophys. J. Lett.* **745**, LL6. [DOI](#).
- Tang, F., Moore, R.L.: 1982, *Solar Phys.* **77**, 263. [DOI](#).
- Tian, H., Xia, L.D., Li, S.: 2008, *Astron. Astrophys.* **489**, 741. [DOI](#).
- Ugarte-Urra, I., Doyle, J.G., Del Zanna, G.: 2005, *Astron. Astrophys.* **435**, 1169. [DOI](#).
- Wang, H., Liu, C.: 2012, *Astrophys. J.* **760**, 101. [DOI](#).
- Wyper, P.F., DeVore, C.R.: 2015. [arXiv](#).
- Yang, S., Zhang, J., Xiang, Y.: 2014, *Astrophys. J. Lett.* **793**, L28. [DOI](#).
- Yang, L., He, J., Peter, H., Tu, C., Zhang, L., Feng, X., *et al.*: 2013, *Astrophys. J.* **777**, 16. [DOI](#).
- Yokoyama, T., Shibata, K.: 1996, *Publ. Astron. Soc. Japan* **48**, 353. [DOI](#).
- Zhang, P., Fang, C., Zhang, Q.: 2012, *Sci. China Phys. Mech. Astron.* **55**, 907. [DOI](#).
- Zhang, Q.M., Ji, H.S.: 2013, *Astron. Astrophys.* **557**, LL5. [DOI](#).
- Zhang, Q.M., Ji, H.S.: 2014a, *Astron. Astrophys.* **561**, AA134. [DOI](#).
- Zhang, Q.M., Ji, H.S.: 2014b, *Astron. Astrophys.* **567**, AA11. [DOI](#).
- Zhang, Q.M., Chen, P.F., Guo, Y., Fang, C., Ding, M.D.: 2012, *Astrophys. J.* **746**, 19. [DOI](#).
- Zhang, Q.M., Chen, P.F., Ding, M.D., Ji, H.S.: 2014, *Astron. Astrophys.* **568**, AA30. [DOI](#).